

Tomographic particle image velocimetry

G. E. Elsinga · F. Scarano · B. Wieneke ·
B. W. van Oudheusden

Received: 13 April 2006 / Revised: 4 September 2006 / Accepted: 19 September 2006 / Published online: 11 October 2006
© Springer-Verlag 2006

Abstract This paper describes the principles of a novel 3D PIV system based on the illumination, recording and reconstruction of tracer particles within a 3D measurement volume. The technique makes use of several simultaneous views of the illuminated particles and their 3D reconstruction as a light intensity distribution by means of optical tomography. The technique is therefore referred to as tomographic particle image velocimetry (tomographic-PIV). The reconstruction is performed with the MART algorithm, yielding a 3D array of light intensity discretized over voxels. The reconstructed tomogram pair is then analyzed by means of 3D cross-correlation with an iterative multigrid volume deformation technique, returning the three-component velocity vector distribution over the measurement volume. The principles and details of the tomographic algorithm are discussed and a parametric study is carried out by means of a computer-simulated tomographic-PIV procedure. The study focuses on the accuracy of the light intensity field reconstruction process. The simulation also identifies the most important parameters governing the experimental method and the tomographic algorithm parameters, showing their effect on the reconstruction accuracy. A computer simulated experiment of a 3D particle motion field describing a vortex ring demon-

strates the capability and potential of the proposed system with four cameras. The capability of the technique in real experimental conditions is assessed with the measurement of the turbulent flow in the near wake of a circular cylinder at Reynolds 2,700.

1 Introduction

The instantaneous measurement of the 3D velocity field is of great interest to fluid mechanic research as it enables to reveal the complete topology of unsteady coherent flow structures. Moreover, 3D measurements are relevant for those situations where the flow does not exhibit specific symmetry planes or axes and several planar measurements are required for a sufficient characterization. In particular this applies to flow turbulence, which is intrinsically 3D and its full description therefore requires the application of measurement techniques that are able to capture instantaneously its 3D structure, the complete stress tensor and the vorticity vector. The advent of PIV and its developments (stereo-PIV, Arroyo and Greated 1991; dual-plane stereo-PIV, Kähler and Kompenhans 2000) showed the capability of the PIV technique to quantitatively visualize complex flows. Several different methods were also proposed to achieve a 3D version of the technique (scanning light sheet, Brücker 1995; holography, Hinsch 2002; 3D PTV, Maas et al. 1993).

A novel system for 3D velocity measurements based on tomographic reconstruction of the 3D particle distribution is investigated in the present study. Recordings of particle images from an illuminated volume taken from several viewing directions simultaneously

G. E. Elsinga (✉) · F. Scarano · B. W. van Oudheusden
Department of Aerospace Engineering,
Delft University of Technology, Kluyverweg 1,
Delft 2629 HS, The Netherlands
e-mail: g.e.elsinga@tudelft.nl

B. Wieneke
LaVision GmbH, Göttingen, Germany

are used to reconstruct the 3D light intensity distribution. The method is therefore referred to as tomographic particle image velocimetry (tomographic-PIV). Provided that two subsequent exposures of the particle images are obtained, the measurement technique returns the instantaneous velocity field within the measurement volume by means of 3D particle pattern cross-correlation.

The motivation for such a 3D PIV system is presented in the next section together with an overview of current alternative techniques. Then the working principle and the tomographic reconstruction method are discussed in detail, followed by a numerical simulation study assessing the effect of the relevant experimental and reconstruction parameters and the full-scale capabilities of tomographic-PIV. The study concludes with the application of the proposed technique to a cylinder wake flow in the turbulent regime. The measurement of 3D coherent structures within the wake is discussed and assessed.

2 Current 3D PIV techniques

Among the different 3D velocimetry techniques presently available holographic-PIV has received most attention (Hinsch 2002; Chan et al. 2004). It uses the interference pattern of a reference light beam with light scattered by a particle, which is recorded on a hologram, to determine the particle location in depth. The in-plane position in principle is given by the position of the diffraction pattern in the image. Illumination of the hologram with the reference light beam reproduces the original light intensity field in the measurement volume at the time of recording, the intensity being highest at the original particle location. The reconstructed intensity field is scanned by a sensor, e.g. a CCD, to obtain a digital intensity map, which can be used for cross-correlation yielding the velocity field. So far holographic-PIV has shown a great potential in terms of a high data yield. However, its drawbacks are that the recording medium is a holographic film requiring wet processing, which makes the process time consuming and somehow inaccurate due to misalignment and distortion when repositioning the hologram for the object reconstruction. The technique was successfully applied to measure a vortex ring in air, the wake of a mixing tab in water (Pu and Meng 2000), a cylinder wake flow in air and a free air nozzle flow (Herrmann et al. 2000) returning large numbers of vectors (up to 92,000 using individual particle pairing, Pu and Meng 2000).

Instead of recording on a photographic plate, the hologram can also be captured directly by a CCD

sensor (Digital-Holographic-PIV, Coëtmelec et al. 2001). In that case the light intensity distribution in the measurement volume is evaluated numerically, usually by solving the Fresnel diffraction formula on the hologram (near-field diffraction, Pan and Meng 2002). CCD sensors, however, have a very limited spatial resolution compared to the photographic plate returning about 2 to 3 orders less particle images and velocity vectors. Moreover, the large pixel pitch requires that the recording is obtained at a relatively small angle (a few degrees between reference beam and scattered light) in order to resolve the interference pattern, hence strongly limiting the numerical aperture and depth resolution (Hinsch 2002).

The scanning-PIV technique is directly derived from standard 2C or stereo PIV with the light sheet scanning through the measurement volume (Brücker 1995). The volume is sliced by the laser sheet at sequential depth positions where the particle image pattern is recorded. The second recording at that depth position can be taken either directly after the first or after the complete scan of the volume. The procedure returns planar velocity fields obtained slightly shifted in space and time, which can be combined to return a 3D velocity field. The strong point of this technique is the high in-plane spatial resolution and the fact that the analysis of the recordings is straightforward. However, scanning-PIV requires high-repetition systems (kHz) to ensure that the complete volume recording is almost simultaneous. The underlying hypothesis of scanning-PIV is that the volume scanning time needs to be small if compared with the characteristic time scale of the investigated flow structure. Cameras with high a recording rate are thus required, which is not a problem in low speed flow as shown by Hori and Sakakibara (2004) measuring a turbulent jet in water. However, the technique is unsuited for air flows and in particular in high speed flows. Moreover, high repetition rate lasers are expensive and provide relatively low pulse energy. It should also be remarked that the experimental setup is significantly more complicated by the addition of a scanning mechanism.

As an alternative to scanning, dual plane stereo PIV (Kähler and Kompenhans 2000) records the particle images in different planes simultaneously using light polarization or different colors to distinguish the scattered light from the two planes. In principle, measurements can be performed over more than two planes with each plane requiring a double-pulse laser, however separation by polarization is the most commonly adopted solution and is possible only over two planes. Furthermore, using different colors complicates the optical arrangement.

Relatively recent options are 3D PTV (Maas et al. 1993) and defocusing PIV (Pereira et al. 2000). These techniques rely on the identification of individual particles in the PIV recordings. The exact position of the particle within the volume is given by the intersection of the lines of sight corresponding to a particle image in the recordings from several viewing directions (typically three or four). The implementation of the particle detection and location varies with the methods. In comparison with the previous two methods, the 3D-PTV approach offers the advantage of being fully digital and fully 3D without the requirement for moving parts. The velocity distribution in the volume is obtained from either particle tracking or by 3D-cross-correlation of the particles pattern (Schimpf et al. 2003). However, the procedure for individual particle identification and pairing can be complex and as it is common for planar PTV several algorithms have been proposed, which significantly differ due to the problem-dependent implementation. The main limitation reported in literature is the relatively low seeding density to which these techniques apply in order to keep a low probability of false particle detection and of overlapping particle images. Moreover, the precision of the volume calibration or in the description of the imaging optics is finite. This means the lines of sight for a particle almost never truly intersect and an intersection criterion is needed. Consequently the maximum seeding density in 3D PTV is kept relatively low. Maas et al. (1993) report a seeding density of typically 0.005 particles per pixel for a three camera system.

The development of the proposed tomographic-PIV technique is motivated by the need to achieve a 3D measurement system that combines the simple optical arrangement of the photogrammetric approach with a robust particle volume reconstruction procedure, which does not rely on particle identification. As a consequence the seeding density can be increased, with respect to 3D PTV, to around 0.05 particles per pixel (as will be shown later), which is not far from the particle image density used in planar experiments. As a consequence the flow field within the 3D domain can be represented with a number of velocity vectors comparable or slightly higher than obtained in planar PIV. Furthermore, the proposed technique features the instantaneous flow field measurement, as opposed to scanning PIV, opening the possibility to perform 3D measurements in several conditions irrespective of the flow velocity. Finally the introduction of high-repetition rate PIV hardware is expected to further extend the measurement technique capability to a 3D time-resolved flow diagnostic tool as already demonstrated in a recent study (Schröder et al. 2006).

3 Working principle of tomographic-PIV

The working principle of tomographic-PIV is schematically represented in Fig. 1. Tracer particles immersed in the flow are illuminated by a pulsed light source within a 3D region of space. The scattered light pattern is recorded simultaneously from several viewing directions using CCD cameras similar to stereo-PIV, applying the Scheimpflug condition between the image plane, lens plane and the mid-object-plane. The particles within the entire volume need to be imaged in focus, which is obtained by setting a proper $f/\#$. The 3D particle distribution (the object) is reconstructed as a 3D light intensity distribution from its projections on the CCD arrays. The reconstruction is an inverse problem and its solution is not straightforward since it is in general underdetermined: a single set of projections can result from many different 3D objects. Determining the most likely 3D distribution is the topic of tomography (Herman and Lent 1976), which is addressed in

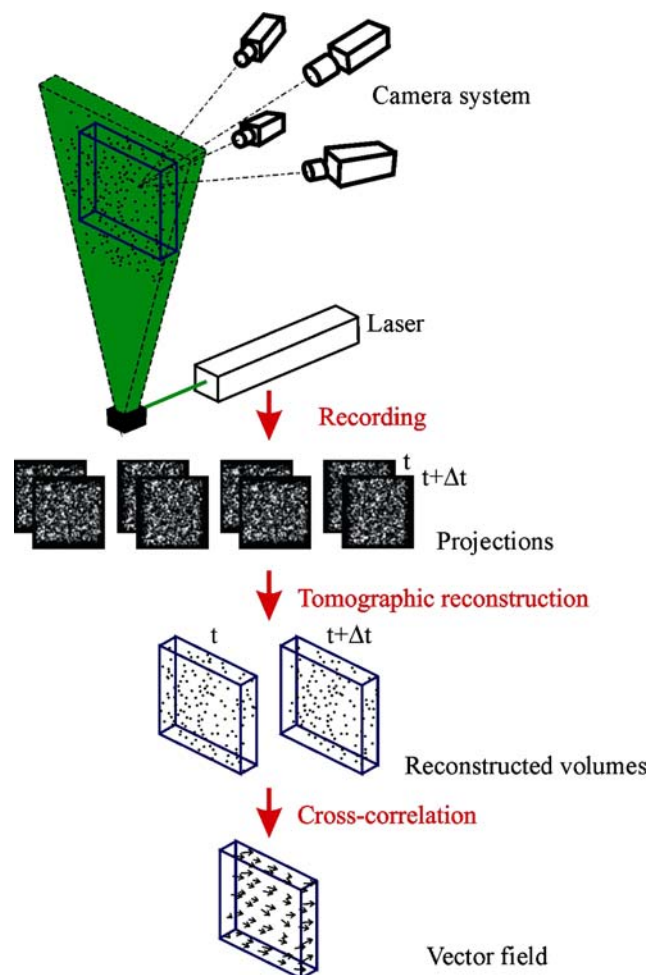


Fig. 1 Principle of tomographic-PIV

the following section. The particle displacement (hence velocity) within a chosen interrogation volume is then obtained by the 3D cross-correlation of the reconstructed particle distribution at the two exposures. The cross-correlation algorithm is based on the cross correlation analysis with the iterative multigrid window (volume) deformation technique (*WIDIM*, Scarano and Riethmuller 2000) extended to 3D.

The relation between image (projection) coordinates and the physical space (the reconstruction volume) is established by a calibration procedure common to stereo PIV. Each camera records images of a calibration target at several positions in depth throughout the volume. The calibration procedure returns the viewing directions and field of view. The tomographic reconstruction relies on accurate triangulation of the views from the different cameras. The requirement for a correct reconstruction of a particle tracer from its images sets the accuracy for the calibration to a fraction of the particle image size (see Sect. 5). Therefore, a technique for the a-posteriori correction for the system misalignment can significantly improve the accuracy of reconstruction (Wieneke 2005). The mapping from physical space to the image coordinate system can be performed by means of either camera pinhole model (Tsai 1986) or by a third-order polynomial in x and y (Soloff et al. 1997).

4 Tomographic reconstruction algorithm

The novel aspect introduced with tomographic-PIV is the reconstruction of the 3D particle distribution by optical tomography. Therefore, a separate section is devoted to the tomographic reconstruction problem and algorithms for solving it.

By considering the properties of the measurement system, it is possible to select a-priori the reconstruction method expected to perform adequately for the given problem. First the particle distribution is discretely sampled on pixels from a small number of viewing directions (typically 3 to 6 CCD cameras) and secondly it involves high spatial frequencies. In these conditions algebraic reconstruction methods are more appropriate with respect to analytical reconstruction methods, such as Fourier and back-projection methods (Verhoeven 1993). For this reason, only the former class of methods is considered for further evaluation.

4.1 Algebraic methods

Algebraic methods (Herman and Lent 1976) iteratively solve a set of linear equations modeling the imaging

system. In the present approach the measurement volume containing the particle distribution (the object) is discretized as a 3D array of cubic voxel elements in (X, Y, Z) (in tomography referred to as the basis functions) with intensity $E(X, Y, Z)$. A cubic voxel element has a uniform non-zero value inside and zero outside and its size is chosen comparable to that of a pixel, because particle images need to be properly discretized in the object as it is done in the images. Moreover, the interrogation by cross-correlation can be easily extended from a pixel to a voxel based object. Then the projection of the light intensity distribution $E(X, Y, Z)$ onto an image pixel (x_i, y_i) returns the pixel intensity $I(x_i, y_i)$ (known from the recorded images), which is written as a linear equation:

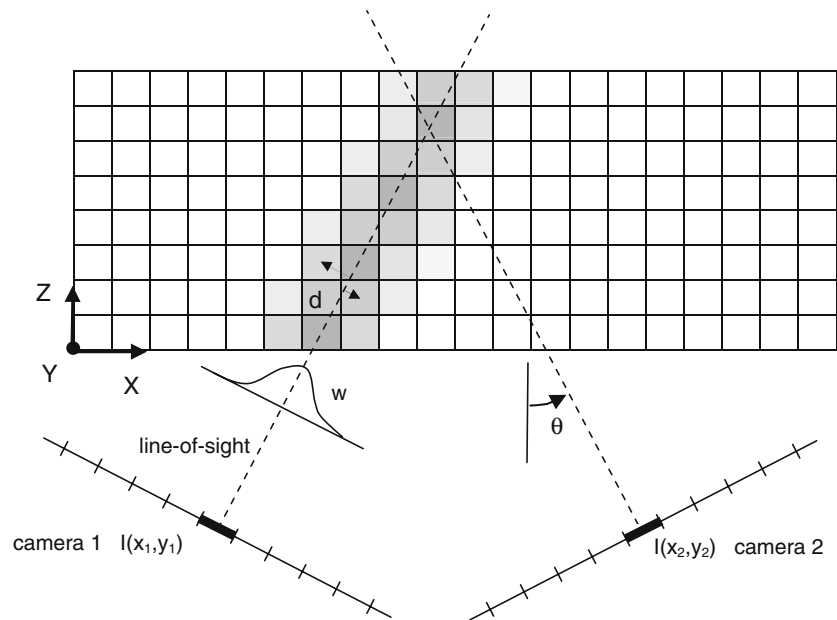
$$\sum_{j \in N_i} w_{ij} E(X_j, Y_j, Z_j) = I(x_i, y_i), \quad (1)$$

where N_i indicates the voxels intercepted or in the neighborhood of the line of sight corresponding to the i th pixel (x_i, y_i) (shaded voxels in Fig. 2). The weighting coefficient w_{ij} describes the contribution of the j th voxel with intensity $E(X_j, Y_j, Z_j)$ to the pixel intensity $I(x_i, y_i)$ and is calculated as the intersecting volume between the voxel and the line of sight (having the cross sectional area of the pixel) normalized with the voxel volume. The coefficients depend on the relative size of a voxel to a pixel and the distance between the voxel center and the line of sight (distance d in Fig. 2). Note that $0 \leq w_{ij} \leq 1$ for all entries w_{ij} in the 2D array W and that W is very sparse, since a line of sight intersects with only a small part of the total volume. The weighting coefficients can also be used to account for different camera sensitivities, forward or backward scatter differences or other optical dissimilarities between the cameras. Alternatively the recorded images can be pre-process in an appropriate way to compensate for these effects.

In the above model, applying geometrical optics, the recorded pixel intensity is the object intensity $E(X, Y, Z)$ integrated along the corresponding line of sight. In that case the reconstructed particle is represented by a 3D Gaussian-type blob, which projection in all directions is the diffraction spot.

A range of algebraic tomographic reconstruction algorithms is available to solve these equations. However, due to the nature of the system, the problem is underdetermined (Sect. 3) and the calculation may converge to different solutions, which implies that these algorithms solve the set of equations of Eq. 1 under different optimization criteria. A detailed discussion and analysis of these optimization criteria is

Fig. 2 Representation of the imaging model used for tomographic reconstruction. In this *top-view* the image plane is shown as a line of pixel elements and the measurement volume is a 2D array of voxels. The *gray level* indicates the value of the weighting coefficient ($w_{i,j}$) in each of the voxels with respect to the pixel $I(x_1, y_1)$



beyond the scope of the present study and can be found in Herman and Lent (1976). Instead the performance of two different tomographic algorithms is evaluated by numerical simulations of a tomographic-PIV experiment focusing the evaluation upon the reconstruction accuracy and convergence properties. The comparison is performed between the additive and multiplicative techniques referred to as ART (algebraic reconstruction technique) and MART (multiplicative algebraic reconstruction technique), respectively (Herman and Lent 1976). Starting from a suitable initial guess ($E(X, Y, Z)^0$ is uniform, see next section) the object $E(X, Y, Z)$ is updated in each full iteration as:

1. for each pixel in each camera i :
2. for each voxel j :

ART: $E(X_j, Y_j, Z_j)^{k+1}$

$$= E(X_j, Y_j, Z_j)^k + \mu \frac{I(x_i, y_i) - \sum_{j \in N_i} w_{i,j} E(X_j, Y_j, Z_j)^k}{\sum_{j \in N_i} w_{i,j}^2} w_{i,j}$$

(2)

MART: $E(X_j, Y_j, Z_j)^{k+1}$

$$= E(X_j, Y_j, Z_j)^k \left(\frac{I(x_i, y_i)}{\sum_{j \in N_i} w_{i,j} E(X_j, Y_j, Z_j)^k} \right)^{\mu w_{i,j}}$$

(3)

end loop 2

end loop 1

where μ is a scalar relaxation parameter, which for ART is between 0 and 2 and for MART must be ≤ 1 . In ART the magnitude of the correction depends on the residual $I(x_i, y_i) - \sum_{j \in N_i} w_{i,j} E(X_j, Y_j, Z_j)$ multiplied by a scaling factor and the weighting coefficient, so that only the elements in $E(X, Y, Z)$ affecting the i th pixel are updated. Alternatively in MART the magnitude of the update is determined by the ratio of the measured pixel intensity I with the projection of the current object $\sum_{j \in N_i} w_{i,j} E(X_j, Y_j, Z_j)$. The exponent again ensures that only the elements in $E(X, Y, Z)$ affecting the i th pixel are updated. Furthermore, the multiplicative MART scheme requires that E and I are definite positive.

4.2 2-D numerical assessment

A domain with reduced dimensionality was adopted to evaluate the performances of the two methods: a $50 \times 10 \text{ mm}^2$ 2D slice of the 3D volume. The 2D particle field contains 50 particles, which images are recorded by three linear array cameras with 1,000 pixel. For the ART reconstruction the relaxation parameter is set at 0.2 and the initial condition is a uniform zero intensity distribution, while for MART relaxation and initial condition are both 1.

The reconstructed particle fields after 20 iterations are shown in Fig. 3. The maximum intensity is 75 counts and values below 3 counts are blanked for readability. The ART algorithm leaves traces of the particles along the lines of sight, while the MART reconstruction shows more distinct particles. The

additive ART scheme works similar to an OR-operator: in order to have a non-zero intensity in the object it is sufficient to have a particle at the corresponding location in one of the PIV recordings. Still the intensity is highest at the actual particle locations. The multiplicative MART scheme behaves as AND-operator: non-zero intensity only at locations where a particle appears in all recordings. The suitability of MART to reconstruct objects with sharp gradients or spikes has been confirmed by Verhoeven (1993). In conclusion, the artifacts in the ART reconstruction are undesirable, especially considering that the signal has to be cross-correlated for interrogation to provide the desired velocity (displacement) information. The result from the MART algorithm better suits tomographic-PIV. Moreover, Fig. 4 shows that the individual particles reconstructed with MART are reconstructed at the correct position with an intensity distribution slightly elongated in depth ($dz \sim 1.5dx$ for the present case).

Besides the sequential update algorithms of Eqs. 2 and 3 schemes that update the reconstructed object simultaneously at every pixel exist, using all equations in a single step, such as the conjugate gradient method (additive scheme) as well as several implementations of the simultaneous MART algorithm (Mishra et al. 1999). Those methods return similar results and are potentially computationally more efficient. The investigation of those methods goes beyond the scope of the present study and may be the subject of further investigations.

5 Parametric study

This section discusses the effect of experimental and algorithm parameters on the reconstruction based on

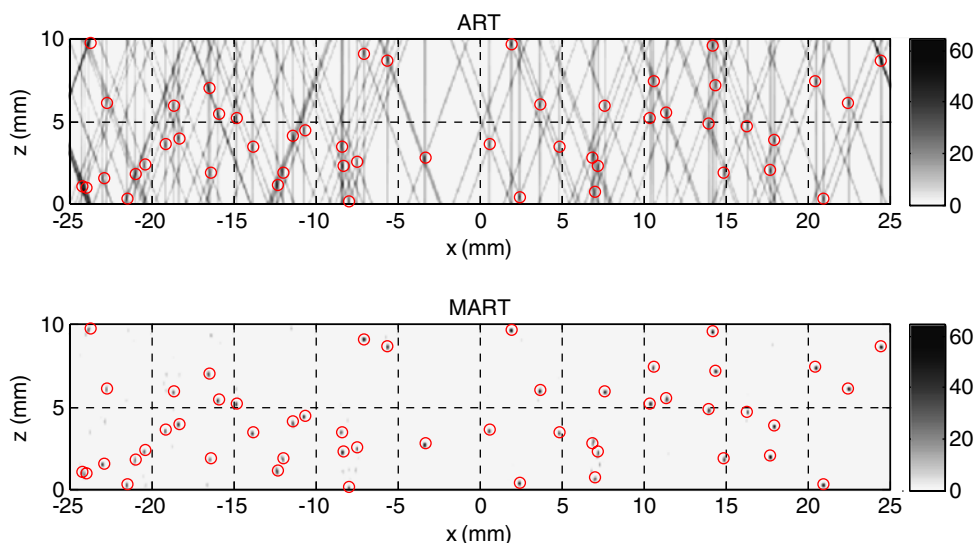
numerical simulations. The number of iterations, the number of cameras, the viewing directions, the particle image density, the calibration accuracy and the image noise are considered.

In the simulation the order of the problem is reduced from a 3D volume with 2D images to a 2D slice with 1D images, which simplifies the computation and the interpretation of the results without losing generality on the results. In fact the 2D volume can be seen as a single slice selected from a 3D volume and similarly the 1D image as a single row of pixels taken from a 2D image.

Tracer particles are distributed in a $50 \times 10 \text{ mm}^2$ slice, which is imaged along a line of 1,000 pixels from different viewing directions θ (Fig. 2) by cameras placed at infinity, such that magnification and viewing direction are constant over the field of view and the magnification is identical for all views and close to 1. Furthermore, the entire volume is assumed to be within the focal depth. Given the optical arrangement the particle location in the images is calculated and the application of diffraction (particle diameter is 3 pixels, which is justified by the large $f/\#$ required) results in the synthetic recordings. The particle image intensity is assumed uniform. The 2D particle field is reconstructed from these recordings at $1,000 \times 200$ voxel resolution using the MART algorithm described in the previous section. Unless stated otherwise the following (baseline) experimental parameters are assumed: three cameras at $\theta = \{-20, 0, 20\}$ degrees, 50 particles (0.05 particles per pixel), 5 reconstruction iterations and no calibration errors or image noise.

To quantify the accuracy of the reconstruction process, the reconstructed object $E_I(X, Z)$ is compared with the exact distribution of light intensity $E_\theta(X, Z)$

Fig. 3 Particle field reconstructed using ART (top) and the same field reconstructed using MART (bottom). The actual particle positions are indicated by circles. The gray level represents the intensity level



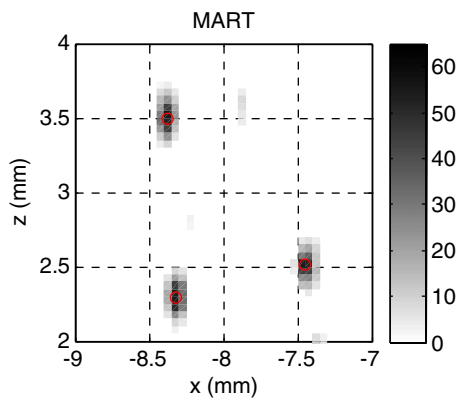


Fig. 4 Detail of the MART reconstruction (Fig. 3) showing individual particles

where the particles are represented by a Gaussian intensity distribution of three voxel diameter. The reconstruction quality Q is defined as the normalized correlation coefficient of the exact and reconstructed intensity distribution, according to:

$$Q = \frac{\sum_{X,Z} E_1(X, Z) \cdot E_0(X, Z)}{\sqrt{\sum_{X,Z} E_1^2(X, Z) \cdot \sum_{X,Z} E_0^2(X, Z)}} \quad (4)$$

A direct estimate of the correlation coefficient to be expected in the cross-correlation analysis of the reconstructed objects is therefore given by Q^2 in the assumption of perfect cross-correlation of the corresponding Gaussian particle fields and uncorrelated reconstruction noise.

First the convergence of the residual and the reconstruction is considered. The residual (Fig. 5, left) decreases monotonically in the tomographic iterative process. Although this behavior does not guarantee that the reconstructed object converges to the exact solution (Watt and Conery 1993), for the present reconstruction algorithm and noise free recordings, the solution converges correctly as evident from Fig. 5, right. A small tendency to divergence after four to five iterations was observed only for a noise level in the recordings in excess of 50% with respect to the particle peak intensity. Such divergence can be countered by applying a smaller relaxation ($\mu = 0.2$) as suggested by Mishra et al. (1999), although that requires more iterations to reach a similar reconstruction quality Q . In the present parametric study and in the experiments presented in Sect. 7 the reconstruction process is stopped after five iterations since both the residual and reconstruction quality Q do not change significantly performing further iterations. Moreover, any divergence phenomenon is avoided. Furthermore, the

experimental results show that with additional iterations the returned vector field changes only within the noise level.

Figure 6 shows the dependence of the reconstruction quality Q on the most relevant experimental parameters, namely the number of cameras, the viewing angle, the particle image density (in particles per pixel), and the calibration error. The diagrams show clear trends, which provides the experimentalist with a first indication of the optimum experimental arrangement and the limitations of the system. A correlation coefficient of 75% with respect to the exact spatial distribution ($Q = 0.75$ corresponding to an expected cross-correlation coefficient of $Q^2 = 0.56$) is used as a cut-off value, above which the reconstruction should be considered sufficiently accurate.

The effect of the number of cameras is clear: adding camera gives additional information on the object, which increases reconstruction accuracy. A 2-camera system ($\theta = -20^\circ$ and 20°) is largely insufficient, whereas Q rapidly increases going to three and four cameras ($\theta = -20^\circ, 0^\circ, 20^\circ$ and 40°) and approaches unity with five cameras ($\theta = -40^\circ, -20^\circ, 0^\circ, 20^\circ$ and 40°).

The viewing angles are changed maintaining the symmetric camera arrangement. The angle indicated in Fig. 6 is the angle between the outer cameras and the z -axis. The graph shows an optimum near 30° . For smaller angles the depth resolution decreases resulting in elongation of the reconstructed-particle in depth. For larger angles the intercepted length of the line-of-sight increases, which causes a larger number of particle to be formed with respect to those actually present in the illuminated volume. Such extra particles will be referred to as “ghost particles” (Maas et al. 1993). This is a problem of ambiguity, which increases with the number of particles, the particle diameter and the length of the line of sight in the volume. The latter increases with the viewing angle in the present configuration, hence the increase in ghost particles. The configurations returning an optimum have a viewing angle in the range of $15\text{--}45^\circ$.

An increased particle density produces a larger percentage of ghost particles consequently decreasing the reconstruction quality. On the other hand, the larger number of particles allows a higher spatial sampling rate of the flow, returning a potentially higher spatial resolution. Therefore, a high particle density is desirable. Based on the simulation results (Fig. 6) the maximum imaged particle density yielding an acceptable reconstruction quality is 0.075 and 0.15 particles per pixel for the three and four camera system, respectively. In a 3D system this would approximately

Fig. 5 Convergence of the normalized residual (*left*) and the reconstruction quality (*right*)

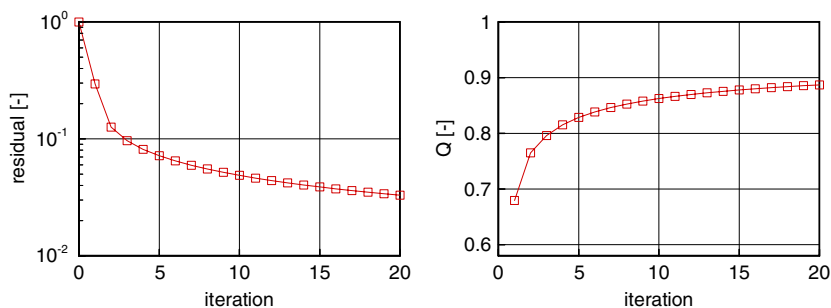
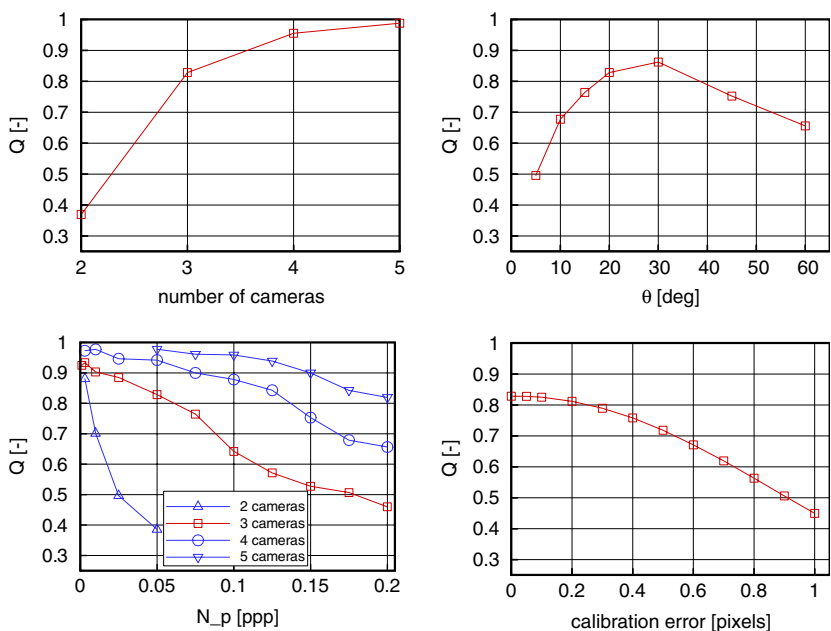


Fig. 6 Reconstruction quality Q as a function of number of cameras (*top-left*), viewing direction (*top-right*), particle density (*bottom-left*) and calibration accuracy (*bottom-right*)



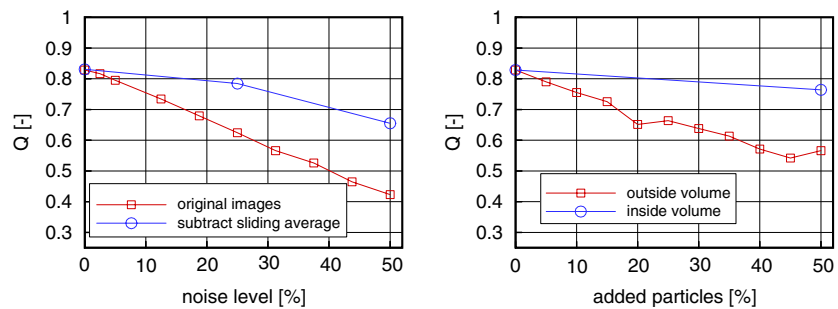
translate to 0.025 and 0.05 particles per pixel assuming each particle image spans three pixel lines. Moreover, Fig. 6-lower-left shows that additional cameras (in the configuration mentioned above) allow a higher seeding density for a given reconstruction quality.

In actual experiments calibration errors may occur, which result in a dislocation of the lines of sight in the reconstruction. As shown by Watt and Conery (1993) this reduces the accuracy of the reconstruction. To quantify the error and to find the necessary calibration accuracy, a calibration error is introduced after recording the images displacing the center-camera towards the right and the right-camera to the left by an equal amount (being the calibration error). Lines of sight from the different cameras that originally intersected now form a triangle in the reconstruction volume. As seen from Fig. 6 a calibration error of 0.4 pixel is the maximum acceptable for an accurate reconstruction. Stereo PIV calibration methods meeting this requirement have been developed for planar

Stereo-PIV (Scarano et al. 2005; Wieneke 2005), which can reduce calibration errors to less than 0.1 pixel.

Finally two types of image noise are considered: random noise added to the recordings and background particles, which are located outside the reconstruction volume. Figure 7-left shows the effect of random noise fluctuations, which range is expressed as a percentage of the particle peak intensity. The image noise deteriorates the reconstructed particle shape and increases the number of ghost particles, as noise is mistaken for particles. As a result the reconstruction quality Q strongly deteriorates with increasing random image noise. However, image pre-processing can be applied to reduce the number of ghost particles. Subtracting a sliding average from the recording using a window of 61 pixels significantly improves the reconstruction results (Fig. 7, left). Random image noise up to 25% of the particle peak intensity has only a small effect after pre-processing. For higher noise level (50%) the change of the particle image shape is important and

Fig. 7 Effect on the reconstruction of white image noise (left) and unmatched particles (right)



cannot be recovered by the pre-processing. The effect of added background particles (located outside the volume) is compared with the same amount of particles added inside the volume in Fig. 7-right. This situation occurs when the reconstructed domain does not include all the illuminated particles either because the laser light sheet has a Gaussian profile or because of stray-light and uncontrolled reflections illuminating particles outside of the measurement volume. The particle located outside the volume have a stronger effect compared to the ones inside, therefore the reconstruction should include the entire illuminated volume to yield the best results.

6 Synthetic 3D experiment

The numerical assessment of tomographic-PIV in a 3D configuration is performed by simulation of the particle motion field around a ring vortex. The vortex core is located in the center plane $z = 0$ mm and forms a circle of 10 mm diameter. The analytical expression of the displacement field (in voxel units) d is given by:

$$d = \begin{pmatrix} u \\ v \\ w \end{pmatrix} = \frac{8R}{l} e^{-\left(\frac{r}{l}\right)}, \quad (5)$$

where R is the distance to the voxel-center ring and $l = 2$ mm is a length scale that defines the width of the vortex. The maximum displacement is 2.9 voxels. Inside the $35 \times 35 \times 7$ mm³ measurement volume 24,500 particles are distributed, which are imaged by four cameras placed at infinity. Each camera has a 30° viewing angle (to the left, to the right, upward and downward) and records the images onto 700×700 pixels. Consequently the particle image density is 0.050 particles per pixel. Furthermore, the magnification is 1 and the particle image diameter is 3 pixels.

The measurement volume is reconstructed at $700 \times 700 \times 140$ voxel resolution performing ten iterations and $\mu = 1$. The returned reconstruction quality Q is

0.75. The reconstruction accuracy can be further assessed by counting the number of intensity peaks or particles. Each reconstructed object contains 24,400 actual particles (peaks within 1.5 voxel radius in the correct position) and 91,600 ghost particles considering only peaks values above 10 in arbitrary units. Even though the number of ghost particles exceeds significantly the number of actual tracer particles, their peak intensity I_p is lower as shown by the probability density function of peak intensity (Fig. 8). The expected peak intensity for an actual particle is 70 against 23 for a ghost. Therefore, the contribution of the ghost particles to the cross-correlation map, hence velocity measurement, is limited.

The displacement field is obtained from the reconstructed object using a 3D extension of the WIDIM algorithm (Scarano and Riethmuler 2000) with 41^3 voxels interrogation volumes at 75% overlap. Therefore, each interrogation volume contains on average 25 particle tracers. The measured vector field contains $66 \times 66 \times 10$ vectors shown in Fig. 9-left where the overall motion pattern is well captured. The surface corresponding to a vorticity magnitude of 0.13 voxels/voxel returns the expected torus. Figure 9-right presents the vectors in the cross section at $x = 0.25$ mm with the corresponding vorticity in x -direction (contours), where the flow symmetry and the two vortex

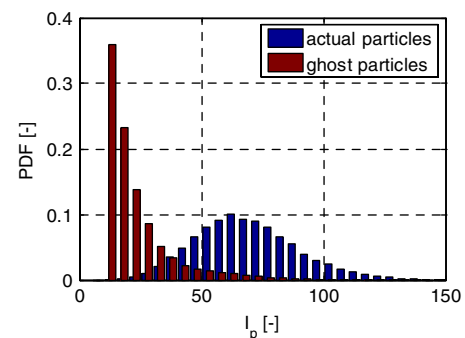


Fig. 8 PDF of particle peak intensity for actual and ghost particles in the reconstructed objects

sections are clearly visible. The normalized cross-correlation peak value is 0.56 and the mean signal-to-noise ratio exceeds 5 indicating a high confidence level for the measurement in such configuration.

The measurement accuracy is presented in the form of 2D scatter plots of the displacement error (Fig. 10), where 90% of the vectors have an absolute error smaller than 0.10 voxels in u and v and less than 0.16 voxels in w (the slightly larger uncertainty in depth direction is due to the 30° viewing direction). The asymmetric scatter plot of the error on the w component (Fig. 10, right) appearing as a bias error results from the limited spatial resolution (modulation error) in combination with the asymmetric w distribution in the flow field. Such bias also appears when cross-correlating the exact distribution of light intensity $E_0(X, Y, Z)$ and is therefore not associated to the reconstruction process.

From the synthetic 3D experiment it can be concluded that tomographic-PIV is capable of the instantaneous measurement of flow structures at a good resolution.

7 Application to a cylinder wake flow

The experimental validation of the technique is performed in a low-speed open-jet wind tunnel with a $0.40 \times 0.40 \text{ m}^2$ square cross section. The wake behind a circular cylinder is measured at $Re_D = 2,700$ where the

diameter D is 8 mm and the free stream velocity is 5 m s^{-1} .

The flow is seeded with $1 \mu\text{m}$ droplets to a particle image density of approximately 0.05 ppp. The illumination source is a Quanta Ray double cavity Nd:YAG laser from Spectra-Physics with a pulse energy of 400 mJ. A knife-edge slit is added in the path of the laser light sheet to cut the low intensity side lobes from the light profile and create a sharply defined illuminated volume of 8 mm thickness. The cylinder axis is oriented vertically, parallel to the laser propagation direction in order to match the largest dimensions of the measurement volume with the streamwise and spanwise coordinates. This choice still allows to measure the Kármán vortices along the wake thickness since the measurement volume is one diameter deep. The time separation between exposures is $35 \mu\text{s}$ yielding a free stream particle displacement of 0.18 mm corresponding to 3.2 voxels.

A four-camera system (Fig. 11) is used to record 12-bit images of the tracer particles at $1,280 \times 1,024$ pixels resolution from different directions. The cameras are equipped with Nikon objectives set at $f/8$. Scheimpflug adapters are used to align the mid-plane of the illuminated area with the focal plane. The effective field of view common to all cameras is $50 \times 50 \text{ mm}^2$. Table 1 lists the properties specific to each camera, such as the magnification M , the focal length f and the viewing angle in x and y -direction θ_x and θ_y , respectively.

Fig. 9 Velocity field and iso-vorticity surface (0.13 voxels/voxel) from a simulation of a vortex ring (left) and velocity vectors in the cross section at $X = 0.25 \text{ mm}$ (right) the contours show the vorticity in x -direction (in voxels/voxel)

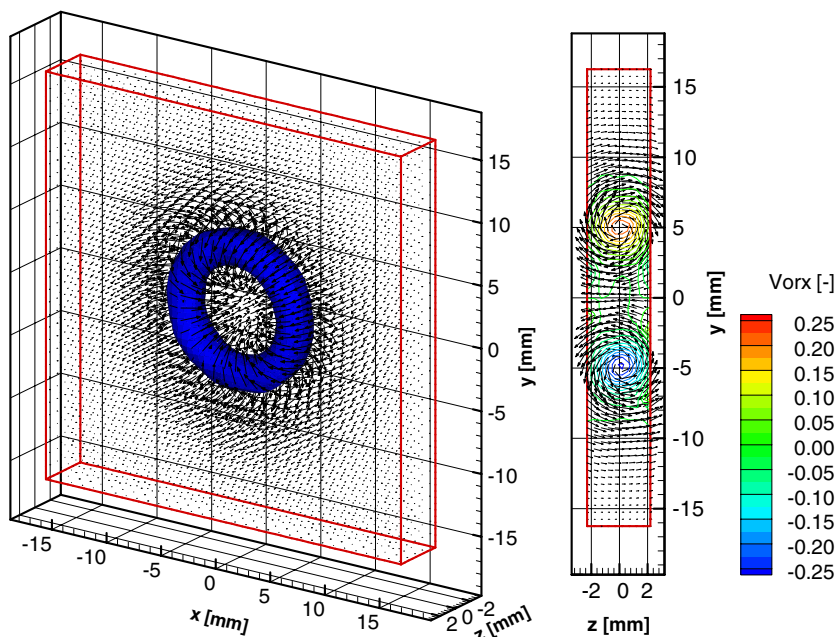


Fig. 10 Scatter plots of the particle displacement error. *Left:* x and y displacement. *Right:* x and z displacement

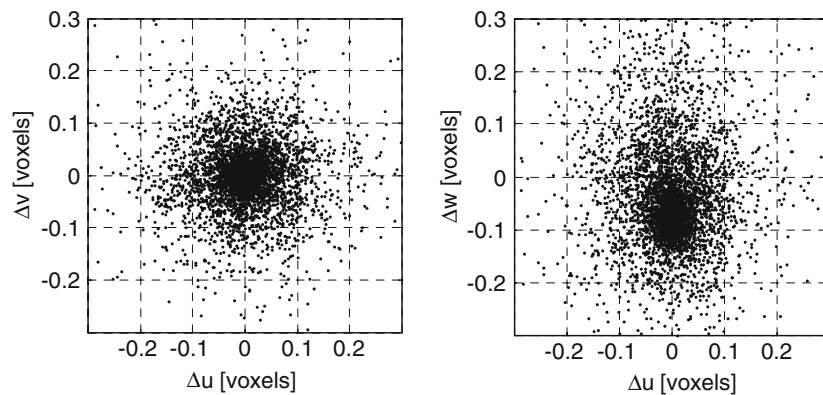
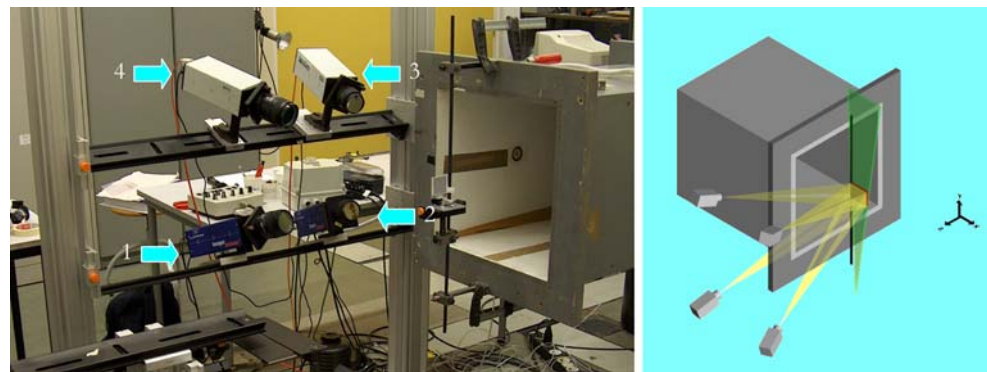


Fig. 11 The optical arrangement for the tomographic-PIV experiments in the low speed wind tunnel



The imaging system is calibrated by scanning a plate with 15×12 marks (crosses) through the volume in depth direction in steps of 4 mm over a total range of 8 mm. In each of the three calibration planes the relation between the physical coordinates (X, Y, Z) and image coordinates is described by a third order polynomial fit. The calibration accuracy is approximately 0.2 pixels. Linear interpolation is used to find the corresponding image coordinates at intermediate z -locations.

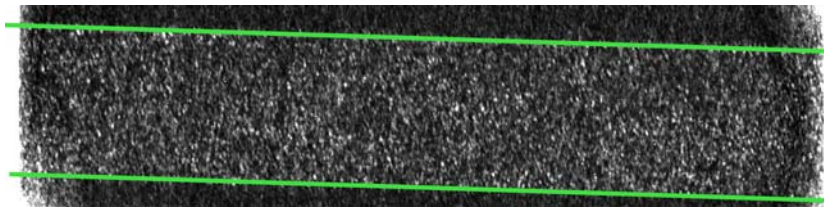
The intensity distribution is reconstructed in a $40 \times 40 \times 10 \text{ mm}^3$ volume discretized with $730 \times 730 \times 184$ voxels using the MART algorithm with five iterations and with the relaxation parameter $\mu = 1$. However, the light sheet thickness covers approximately 150 voxels in depth. The reconstruction process is improved by means of image pre-processing with background intensity removal, particle intensity equalization and a Gaussian smooth (3×3 kernel size).

In real experimental conditions an assessment of the reconstruction quality is not straightforward, since the actual particle distribution is unknown. It is possible, however, to estimate the number and intensity distribution of the ghost particles by comparing the light intensity reconstructed outside and inside the illuminated region (representing reconstruction noise and signal plus noise, respectively). Note that the light sheet position can be clearly identified within the reconstructed volume (Fig. 12) due to the application of a slit in the light path. The results confirm that the expected peak intensity for the ghost particles is lower than for the actual tracer particles (as in Fig. 8). Moreover, the ratio of actual particles over ghost particles is 2 considering only the range of peak intensities corresponding to the actual particles. For further detail on the assessment of reconstruction volumes in real experiments the reader is referred to Elsinga et al. (2006).

Table 1 Optical arrangement

Camera #	Camera type	Pixel pitch (μm)	M (-)	f (mm)	θ_y ($^\circ$)	θ_x ($^\circ$)
1	Imager Intense	6.45	0.13	60	+20	+22
2	Imager Intense	6.45	0.12	50	-10	+22
3	SensiCam	6.7	0.12	50	-10	-22
4	SensiCam QE	6.45	0.14	60	+20	-22

Fig. 12 Top view of the reconstructed volume showing the light intensity integrated in y -direction. The green lines indicate the position of the light sheet



The cross-correlation analysis returned $64 \times 64 \times 30$ velocity vectors using an interrogation volume size of $41 \times 41 \times 21$ voxels with 75% overlap. Data validation based on a signal-to-noise ratio threshold of 1.2 and on the normalized median test with maximum threshold of 2 (Westerweel and Scarano 2005) returns 4% spurious vectors. The average signal-to-noise ratio and normalized correlation coefficient are 3.8 and 0.6, respectively.

An example of an instantaneous velocity distribution is presented in Fig. 13. In the plot the y -axis corresponds to the cylinder axis and the x -coordinate is the distance from the cylinder axis in flow direction. Low velocity and flow reversal is observed for $x/D < 3$ followed by a recovery of the flow velocity to approximately 80% of its free stream value at $x/D = 6$. A large swirling motion due to a Kármán vortex shed from the lower surface of the cylinder is observed around $x/D = 2.8$ and $z/D = -0.2$ (labeled as A in Fig. 13), characterized by a vorticity peak. Besides the Kármán vortices the vorticity iso-surface in Fig. 13 also reveals a number of secondary streamwise vortex structures (indicated by B), which interact with the primary rollers. At the present Reynolds number the shear layers separating from the cylinder are transitional and three-dimensionality on the scale of the Kármán vortices is expected (Williamson 1996).

To improve the visualization of the structural organization of the flow the span wise and the combination of stream wise and z component of vorticity are color-coded in Fig. 14. The four uncorrelated snapshots show different phases of the vortex shedding cycle. The top-left snapshot (corresponding to Fig. 13) contains parts of four Kármán vortices; two from the lower cylinder surface (green) at $x/D = 2.8$ and 6, and two from the upper surface (cyan) at $x/D = 2.5$ and 4.5. The normalized vorticity level in these vortices $\omega_y D/u_\infty = 2.2$ agrees fairly well with the recent planar PIV measurements in the Reynolds number range 2,000 to 10,000 from Huang et al. (2006), who report an average normalized peak vorticity of 2.1 at $x/D = 3$.

The secondary vortex structures are also clearly visible in Fig. 14 (blue and red depending on the orientation of vorticity in stream wise direction) and appear to be organized in counter rotating pairs. Figure 15 shows in detail how the secondary vortices curl in between the primary Kármán vortices. Their effect is to first distort the primary rollers, as observed in the upper two snapshots of Fig. 14 at $x/D = 4.5$, and finally they cause the breakup of the primary vortices. The two snapshots of Fig. 14-bottom show a more regular span wise organization of the secondary vortices yielding a quasi periodic behavior. From a visual inspection the normalized spatial wave length λ_y/D is

Fig. 13 Instantaneous velocity distribution showing one every third vector and vorticity magnitude iso-surface ($|\omega| = 2.3 \times 10^3 \text{ s}^{-1}$)

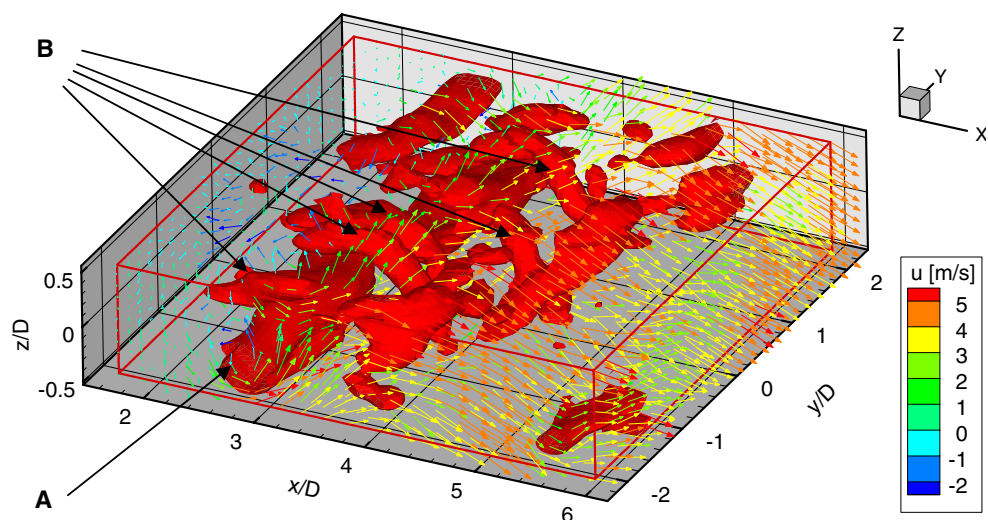


Fig. 14 Instantaneous vorticity iso-surfaces ($\omega = 1.4 \times 10^3 \text{ s}^{-1}$). Color coding: green $\omega_y < 0$; cyan $\omega_y > 0$; blue $\sqrt{\omega_x^2 + \omega_z^2} \cdot \text{sign}(\omega_x) < 0$; red $\sqrt{\omega_x^2 + \omega_z^2} \cdot \text{sign}(\omega_x) > 0$. The cylinder is shown in yellow

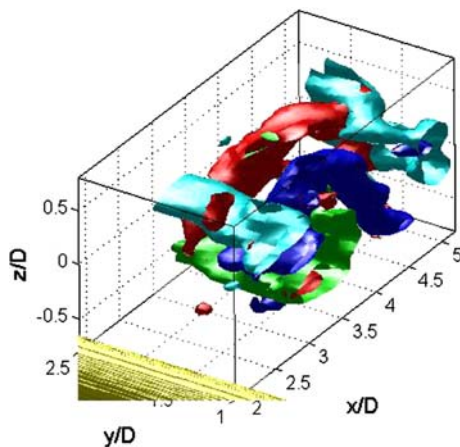
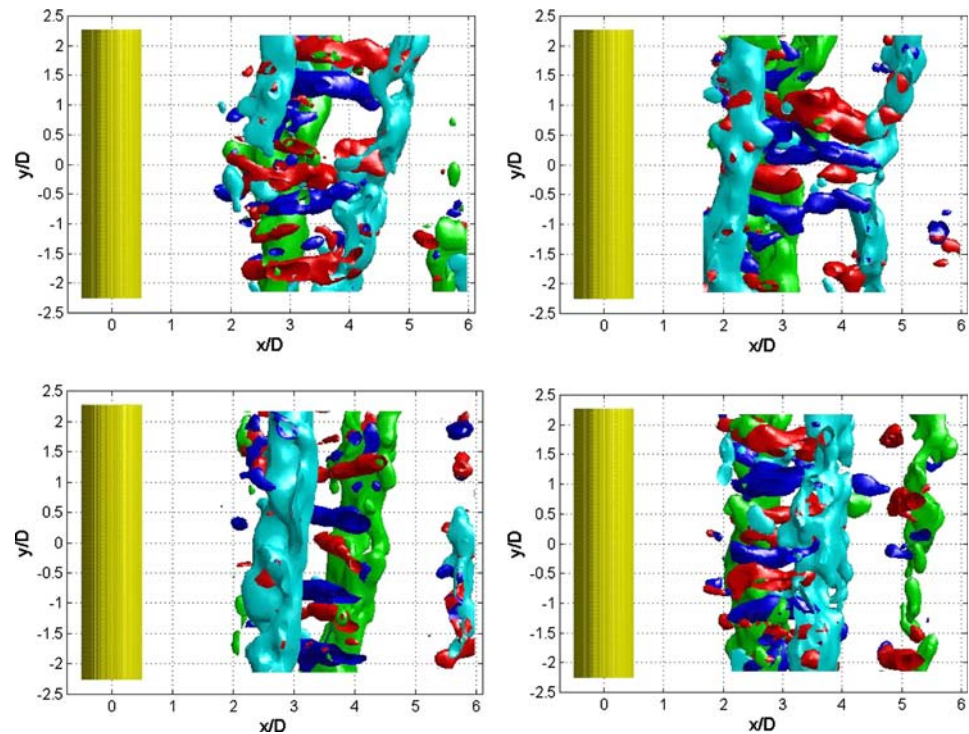


Fig. 15 Detail of the interaction between primary and secondary vortices taken from upper left snapshot of Fig. 14

estimated at 1.2, which is again in good agreement with Huang et al. (2006) and slightly in excess with the reported values at lower Reynolds number (Williamson 1996). A more detailed discussion of the cylinder wake flow is beyond the scope of the present study, but can be found in Scarano et al. (2006).

The flow velocity exhibits a large variation along the viewing directions of the cameras, as shown above, which allows to conclude that independent velocity information is measured along the z -coordinate corresponding with the volume depth. Possible

noise or reconstruction artifacts, when present, are in fact expected to propagate particle (displacement) information along viewing lines ultimately resulting in a quasi-uniform particle displacement along that line. Clearly such effects do not play a dominant role in the current experiment.

Further confidence in the measurement technique is given by recent quantitative comparisons between tomographic- and stereo-PIV, which showed a good agreement of the returned flow statistics (mean and RMS) along profiles in the cylinder wake (Elsinga et al. 2006) and velocity distribution in a vortex ring (Wieneke and Taylor 2006).

8 Conclusions

Tomographic-PIV was introduced as a novel technique for 3D velocity measurements. The 3D particle distribution within a volume is reconstructed by optical tomography from 2D particle image recordings taken simultaneously from several viewing directions. Velocity information results from 3D particle pattern correlation of two reconstructions obtained from subsequent exposures of the particle images. The technique makes use of digital imaging devices as opposed to holographic-PIV, and it allows a typical spatial resolution that is in between 3D-PTV (low seeding density) and scanning-PIV (high seeding density).

Moreover, the technique measures the particle motion instantaneously in the 3D observation domain, which makes it suitable for the analysis of flows in several regimes and irrespective of the flow speed.

A numerical simulation of a tomographic-PIV experiment showed that the multiplicative algebraic reconstruction techniques (MART) are the most suited to particle reconstruction returning distinct particles with limited artifacts. Furthermore, it was shown that the reconstruction algorithm converges to the desired solution for noise free particle image recordings. Based on a parametric study the number of cameras, viewing direction, particle density, calibration accuracy and image noise were identified as critical factors determining the quality of the 3D particle reconstruction. The calibration must be accurate within 0.4 pixel. Image pre-processing (e.g., removing background intensity) reduces the effect of random image noise. Adding a camera to the system provides extra information, which can be used to increase measurement resolution (increasing the particle density) or accuracy.

A 3D simulation of a ring vortex flow showed that the 3D measurement configuration with four cameras can yield $66 \times 66 \times 10$ vectors in a $35 \times 35 \times 7 \text{ mm}^3$ volume, with a typical measurement error of 0.1 pixels.

The application of the technique to a turbulent cylinder wake flow at a Reynolds number $Re_D = 2700$, provided an experimental assessment of the capability of tomographic PIV. The measurement volume was aligned with the cylinder axis returning the streamwise evolution of the wake as well as its spanwise organization within a depth of one cylinder diameter (8 mm). The instantaneous velocity returned the Kármán street with counter-rotating vortices alternatively shed and cross-linked by secondary vortex structures aligned in the streamwise-binormal direction. The results give a further confirmation that the tomographic-PIV technique is suited to the study of complex 3D flows.

Acknowledgments The authors wish to thank Prof. Dave Watt (University of New Hampshire) and Dr. Dirk Michaelis (LaVision GmbH) for the valuable suggestions on optical tomography and for the software development, respectively.

References

- Arroyo MP, Greated CA (1991) Stereoscopic particle image velocimetry. *Meas Sci Technol* 2:1181–1186
- Brücker Ch (1995) Digital-particle-image-velocimetry (DPIV) in a scanning light-sheet: 3D starting flow around a short cylinder. *Exp Fluids* 19:255–263
- Chan VSS, Koek WD, Barnhart DH, Bhattacharya N, Braat JJM, Westerweel J (2004) Application of holography to fluid flow measurements using bacteriorhodopsin (bR). *Meas Sci Technol* 15:647–655
- Coëtmellec S, Buraga-Lefebvre C, Lebrun D, Özkul C (2001) Application of in-line digital holography to multiple plane velocimetry. *Meas Sci Technol* 12:1392–1397
- Elsinga GE, Van Oudheusden BW, Scarano F (2006) Experimental assessment of tomographic-PIV accuracy. In: 13th international symposium on applications of laser techniques to fluid mechanics, Lisbon, Portugal, paper 20.5
- Herman GT, Lent A (1976) Iterative reconstruction algorithms. *Comput Biol Med* 6:273–294
- Herrmann S, Hinrichs H, Hinsch KD, Surmann C (2000) Coherence concepts in holographic particle image velocimetry. *Exp Fluids* 29(7):S108–S116
- Hinsch KD (2002) Holographic particle image velocimetry. *Meas Sci Technol* 13:R61–R72
- Hori T, Sakakibara J (2004) High-speed scanning stereoscopic PIV for 3D vorticity measurement in liquids. *Meas Sci Technol* 15:1067–1078
- Huang JF, Zhou Y, Zhou T (2006) Three-dimensional wake structure measurement using a modified PIV technique. *Exp Fluids* 40:884–896
- Kähler CJ, Kompenhans J (2000) Fundamentals of multiple plane stereo particle image velocimetry. *Exp Fluids* 29:S70–S77
- Maas HG, Gruen A, Papantoniou D (1993) Particle tracking velocimetry in three-dimensional flows. *Exp Fluids* 15:133–146
- Mishra D, Muralidhar K, Munshi P (1999) A robust MART algorithm for tomographic applications. *Num Heat Transfer Part B* 35:485–506
- Pan G, Meng H (2002) Digital holography of particle fields: reconstruction by use of complex amplitude. *Appl Opt* 42:827–833
- Pereira F, Gharib M, Dabiri D, Modarress D (2000) Defocusing digital particle image velocimetry: a 3-component 3-dimensional DPIV measurement technique. *Exp Fluids* 29(7):S78–S84
- Pu Y, Meng H (2000) An advanced off-axis holographic particle image velocimetry (HPIV) system. *Exp Fluids* 29:184–197
- Scarano F, Riethmuller ML (2000) Advances in iterative multigrid PIV image processing. *Exp Fluids* 29:S51–S60
- Scarano F, David L, Bsibsi M, Callaud D (2005) S-PIV comparative assessment: image dewarping + misalignment correction and pinhole + geometric back projection. *Exp Fluids* 39:257–266
- Scarano F, Elsinga GE, Bocci E, Van Oudheusden BW (2006) Investigation of 3-D coherent structures in the turbulent cylinder wake using Tomo-PIV. In: 13th international symposium on applications of laser techniques to fluid mechanics, Lisbon, Portugal, paper 20.4
- Schimpf A, Kallweit S, Richon JB (2003) Photogrammetric particle image velocimetry. In: 5th international symposium on particle image velocimetry, Busan, Korea, paper 3115
- Schröder A, Geisler R, Elsinga GE, Scarano F, Dierksheide U (2006) Investigation of a turbulent spot using time-resolved tomographic PIV. In: 13th international symposium on applications of laser techniques to fluid mechanics, Lisbon, Portugal, paper 1.4
- Soloff SM, Adrian RJ, Liu ZC (1997) Distortion compensation for generalized stereoscopic particle image velocimetry. *Meas Sci Technol* 8:1441–1454
- Tsai RY (1986) An efficient and accurate camera calibration technique for 3D machine vision. In: Proceedings of IEEE conference on computer vision and pattern recognition, Miami Beach, FL, USA, pp 364–374

- Verhoeven D (1993) Limited-data computed tomography algorithms for the physical sciences. *Appl Opt* 32:3736–3754
- Watt DW, Conery DG (1993) Computational aspects of optical tomography for fluid mechanics and combustion. In: 3rd ASME symposium on experimental and numerical flow visualization, New Orleans, LA, USA, pp 241–251
- Westerweel J, Scarano F (2005) A universal detection criterion for the median test. *Exp Fluids* 39:1096–1100
- Wieneke B (2005) Stereo-PIV using self-calibration on particle images. *Exp Fluids* 39:267–280
- Wieneke B, Taylor S (2006) Fat-sheet PIV with computation of full 3D-strain tensor using tomographic reconstruction. In: 13th international symposium on applications of laser techniques to fluid mechanics, Lisbon, Portugal, paper 13.1
- Williamson CHK (1996) Vortex dynamics in the cylinder wake. *Annu Rev Fluid Mech* 28:477–539